Asymmetric modification of cellulose nanocrystals with PAMAM dendrimers for the preparation of pH-responsive hairy surfaces

Maud Chemin, Céline Moreau, Bernard Cathala, Ana Villares

Asymmetric modification of cellulose nanocrystals with PAMAM dendrimers for the preparation of pH-responsive hairy surfaces

Maud Chemin, Céline Moreau, Bernard Cathala, Ana Villares*

INRAE, UR1268 BIA, F-44316, Nantes, France

*maud.chemin@inrae.fr / +33(0)2.40.67.50.18

celine.moreau@inrae.fr / +33(0)2.40.67.51.44

bernard.cathala@inrae.fr / +33(0)2.40.67.50.68

ana.villares@inrae.fr / +33(0)2.40.67.50.18

KEYWORDS: tunicate cellulose nanocrystals; reducing end; dendrimer; PAMAM; quartz crystal microbalance with dissipation (QCM-D); surface plasmon resonance (SPR).

ABSTRACT

In this work, we present a straightforward method to attach a globular dendrimer at the reducing end of cellulose nanocrystals obtained from tunicates (t-CNC). We investigated the first four generations of poly(amidoamine) dendrimers (PAMAMs G0 to G3) to obtain hybrid t-CNCs. Taking advantage of the inherent chemical asymmetry resulting from the parallel organization of cellulose chains in CNCs, we prepared asymmetric nanocrystals by selectively modifying their reducing end. The aggregation behavior of hybrid t-CNCs was studied by dynamic light scattering (DLS) and scanning transmission electron microscopy (STEM); and interactions of these asymmetric nanoparticles with gold surface were elucidated using quartz crystal microbalance with dissipation (QCM-D) and surface plasmon resonance (SPR). Hybrid t-CNCs formed hairy layers onto gold surface combining the properties of rigid rod-like nanocrystals with globular and flexible PAMAM dendrimers. Moreover, the presence of amino groups provided pH-responsive properties to hybrid t-CNCs, and QCM results revealed reversible swelling/deswelling behavior. Thereby, we achieved to synthesize tree-shaped functional bio-based materials that adsorbed on gold and formed pH-responsive hairy surfaces.

1. INTRODUCTION

Cellulose nanocrystals (CNCs) have arisen as promising candidates for high-end materials applications. Besides their high abundance, renewability and low environmental impact, CNCs have outstanding material characteristics, including high tensile strength and barrier properties suitable for composite reinforcement (Habibi, Lucia, & Rojas, 2010), surface properties for emulsion stabilization (Capron, Rojas, & Bordes, 2017), chiral nematic liquid crystal behavior for

optically active materials (Shopsowitz, Qi, Hamad, & MacLachlan, 2010) and colloidal stability for the formation of gels (Lewis, Hatzikiriakos, Hamad, & Maclachlan, 2019; Talantikite, Beury, Moreau, & Cathala, 2019). CNCs are produced from cellulose fibers after removal of the disordered cellulose domains by acid hydrolysis. This leads to rigid, high crystalline nanorods bearing hydroxyl groups on their surface. The particularity of CNCs is the presence of two differentiated chemical ends resulting from the parallel alignment of cellulose I chains (Hieta, Kuga, & Usuda, 1984; Koyama, Helbert, Imai, Sugiyama, & Henrissat, 1997). Thus, the hemiacetal groups allow the asymmetric introduction of non-cellulosic functionalities at the reducing end, enabling novel interactions, self-assembly capacity and new properties. Up to now, only few studies take advantage of the parallel arrangement of cellulose chains to functionalize CNCs in an asymmetric way (Tao, Lavoine, Jiang, Tang, & Lin, 2020). For instance, research has been focused on the grafting of synthetic polymers, such as polyacrylamide, or natural ones, like β-casein, at the reducing end of cellulose nanocrystals (Karaaslan, Gao, & Kadla, 2013; Risteen et al., 2018; Sipahi-Saglam, Gelbrich, & Gruber, 2003; Zoppe et al., 2017). Modification of reducing ends was also implemented to drive the self-assembly of hybrid CNCs. In this field, the introduction of thermoresponsive polyetheramines results in thermally switchable star-like supramolecular assemblies (Lin, Cousin, Putaux, & Jean, 2019). 2D surface adsorption was also achieved using specific interactions, such as biotin/streptavidin (Villares, Moreau, & Cathala, 2018) or thiol/gold (Arcot, Lundahl, Rojas, & Laine, 2014; Arcot et al., 2013). In these cases, hybrid CNCs were found to be adsorbed in an upright orientation leading to cilia-mimetic hairy surfaces. Additionally, recent works used thiol functionalized cellulose nanocrystals for composite reinforcement (Li et al., 2018; Tao, Dufresne, & Lin, 2019).

In this work, we study the functionalization of cellulose nanocrystals from tunicate (t-CNC) at their reducing ends by the introduction of poly(amidoamine) dendrimers (PAMAM). PAMAMs are globular and flexible dendrimers with an ethylenediamine core as illustrated on Fig. 1. They display several primary amine groups on their surface as well as tertiary amine and amide groups in their core whose number increases with generation. They are then responsive to pH changes thanks to the protonation/deprotonation of the amine groups (Lee, Athey, Wetzel, Meixner, & Baker, 2002). Thanks to their pH-responsive properties PAMAM dendrimers have found promising applications in the biomedical field, mostly as molecular vectors and nanoreactors (Crooks, Zhao, Sun, Chechik, & Yeung, 2001; Esfand & Tomalia, 2001; Venditto, Regino, & Brechbiel, 2005).

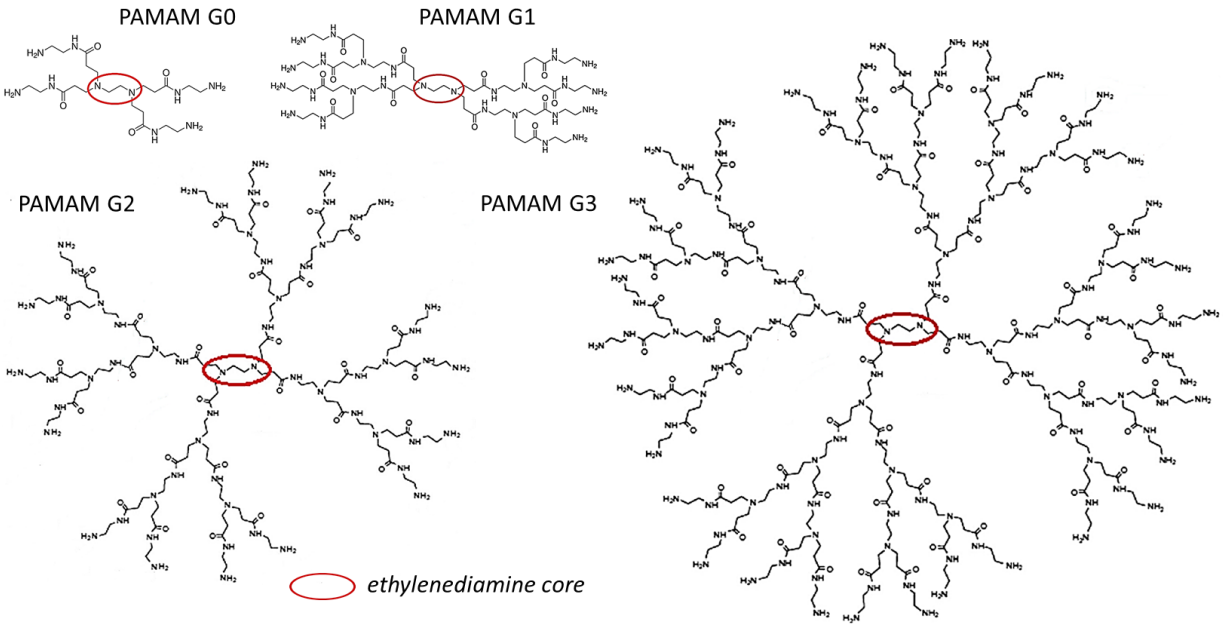

Fig. 1. PAMAM dendrimers chemical structures from generation 0 to generation 3

To the best of our knowledge, few reports on the functionalization of CNCs with PAMAMs are reported. Dadkhah Tehrani and Basiryan studied the chemical surface modification of CNCs

74 from cotton to synthesize step-by-step PAMAM dendrimers up to the 3rd generation (Dadkhah
75 Tehrani & Basiryan, 2015). They showed that the rod-like shape of CNCs was preserved, and
76 that the presence of grafted PAMAMs, as small globular residues covering the CNC surface, was
77 detectable. Chen et al. grafted PAMAM of 6th generation on wood CNCs surface and showed
78 that their aggregation behavior depended on pH (L. Chen, Cao, Grishkewich, Berry, & Tam,
79 2015). Indeed, stable dispersions were obtained at very low or very high pH only to allow
80 electrostatic repulsions from positive or negative charges respectively. They further showed the
81 possibility to load gold nanoparticles in the PAMAMs grafted on CNCs leading to improved gold
82 catalysis activity (Li Chen, Cao, Quinlan, Berry, & Tam, 2015). Very recently, Tavakolian et al.
83 functionalized electrosterically stabilized nanocrystalline cellulose produced from softwood
84 kraft pulp at their both ends using PAMAM 5th generation (Tavakolian et al., 2019). They
85 showed that this system formed 3D structures whose shape depended on the PAMAM
86 concentration.

87 The goal of this work relies on the selective introduction of PAMAM functionalities at the
88 reducing ends of t-CNCs. By selectively grafting this functional dendrimer at the reducing end of
89 t-CNCs, we aim at combining the stretch-compress properties of PAMAMs with the surface
90 properties of cellulose nanorods. We focused on the first four generations of PAMAM
91 dendrimers, from a small molecule (G0) to a globular dendrimer (G3) in order to monitor the
92 properties as a function of the PAMAM generation. We studied the behavior (interactions and
93 assembly) of the obtained hybrid nanoparticles by dynamic light scattering (DLS), quartz crystal
94 microbalance with dissipation (QCM-D) and surface plasmon resonance (SPR). The pH-

responsive properties of the PAMAM-modified t-CNCs adsorbed on the gold surface was evaluated by QCM-D.

2. EXPERIMENTAL

2.1. Materials

Poly(amidoamine) dendrimers (PAMAM Dendrimer Kit, generations 0-3), N-(3-dimethylaminopropyl)-N-ethylcarbodiimide hydrochloride (EDC), N-hydroxysuccinimide (NHS), sodium chlorite ($NaClO_2$), potassium chloride (KCl), potassium hydroxide (KOH), sodium hydroxide (NaOH), hydrochloric acid (HCl 37%), sulfuric acid (H_2SO_4) and acetic acid were purchased from Sigma-Aldrich (France) and were used without further purification. Dialysis membrane, molar mass cut off 12-14 kDa, was purchased from Spectrum Laboratories Inc. Water was purified by Millipore Milli-Q purification system (18.2 MΩ).

2.2. Methods

2.2.1. Cellulose nanocrystals preparation

Tunicate cellulose nanocrystals (t-CNC) were obtained accordingly to our previous work (Villares et al., 2018). Briefly, cellulose pulp from tunicate (*Styela clava*) was boiled in 1% NaOH for 10 h and washed with milli-Q water. The pulp was further purified by a 0.3% $NaClO_2$ treatment at pH 4.9 for 2 h at 70 °C, and washed thoroughly in milli-Q water, similarly to previously described procedures (Favier, Chanzy, & Cavaillé, 1995; Sugiyama, Persson, & Chanzy, 1991). t-CNCs were then obtained by sulfuric acid hydrolysis. To a cooled suspension of tunicate cellulose pulp in water, sulfuric acid was slowly added under vigorous mechanical stirring to reach a final concentration of 65%. The dispersion was kept at 40 °C for 90 min under

117 stirring. The dispersion was cooled to 0°C, filtered over a 0.5 µm fritted glass filter, and washed
118 with milli-Q water until neutrality was reached. Dialysis (molar mass cut off 12-14 kDa) was
119 performed for 15 days. Note that t-CNCs are negatively charged due to sulfate groups at their
120 surface (22±1 µmol g^{-1} (Villares et al., 2018)) which gives a stable colloidal suspension.
121 *2.2.2. Introduction of PAMAM dendrimer at the reducing end of t-CNCs*
122 t-CNCs were functionalized at their reducing end in aqueous medium, following the procedure
123 previously described with minor modifications (Arcot et al., 2014). The aldehyde groups on the
124 reducing end of t-CNCs (50 mL at 6.9 g L^{-1}) were oxidized to carboxyl groups by the addition of
125 8.7 mmol of $NaClO_2$, and the pH was adjusted to 3.5 using acetic acid, followed by stirring for 20
126 h at room temperature. The reaction mixture was purified by centrifugation (20000 g, 20°C, 30
127 min) to remove most of the chloric derivatives and then by dialysis (molar mass cut off 12-14
128 kDa) against milli-Q water for 6 days.
129 A 2 g L^{-1} suspension of t-CNC-COOH (5.8 mL) was degassed by bubbling nitrogen for 20 min, and
130 0.72 µmol of NHS were added, followed by 7.2 µmol of EDC, and the pH was checked to be
131 close to 6.5. Appropriate amounts of KCl were added such that the final suspension was 0.3 M.
132 PAMAM dendrimers were added in large excess to avoid the grafting of several t-CNCs on the
133 same dendrimer. Since the number of amine functions are increasing with the dendrimer
134 generation, decreasing amounts of PAMAMs were added, *i.e.* 72, 36, 18 and 9 µmol for
135 generations 0, 1, 2 and 3, respectively. Then, pH was checked to be more than 9.2. Note that
136 the addition of salt in the suspension would screen negative charges at the t-CNCs surface and
137 PAMAM dendrimers are not positively charged at pH above 9, which must limit PAMAM
138 unspecific adsorption on t-CNC surface. The reaction was incubated under stirring at room

139 temperature for 24 h. PAMAM-functionalized t-CNCs were purified by centrifugation (20000 g,
140 60 min, 20 °C) and then dialyzed (molar mass cut off 12-14 kDa) against Milli-Q water for 14
141 days. After coupling, hybrid nanoparticles are denoted t-CNC-Gx, x being the PAMAM
142 generation number.

143 *2.3 Characterization*

144 *2.3.1. Zeta potential (pZ) and dynamic light scattering (DLS)*

145 *pZ* and DLS experiments were performed with a Malvern NanoZS instrument. All measurements
146 were made at 20 °C with a detection angle of 12.8° and 173° for *pZ* and DLS, respectively. The
147 correlogramms were recorded using Malvern DTS software. t-CNC and hybrid t-CNC-Gx
148 suspensions were diluted to 0.1 g L^{-1} in pure water or in KOH 1 mM and then filtered through 5
149 µm.

150 *2.3.2. Scanning Transmission Electron Microscopy (STEM)*

151 t-CNC and hybrid t-CNC-Gx suspensions were diluted to 0.2 g L^{-1} in pure water or in KOH 1 mM
152 and deposited on freshly glow-discharged carbon-coated electron microscope grids (200 mesh,
153 Delta Microscopies, France). After 1 min, the excess of solvent was removed by blotting
154 (Whatman filter paper). The grids were dried overnight in air at ambient temperature and then
155 coated with platinum layer by an ion-sputter coater (thickness = 0.5 nm). The grids were
156 observed with a Quattro scanning electron microscope (Thermo Scientific) with a STEM
157 detector, working at 10 kV.

158 *2.3.3. Quartz crystal microbalance with dissipation (QCM-D)*

159 The QCM-D measurements were performed with a Q-Sense E4 instrument (AB, Sweden) using a
160 piezoelectric AT-cut quartz crystal coated with gold electrodes on each side (QSX301, Q-Sense).

All measurements were carried out at 20 °C using the QCM flow cell modules. A baseline was first established by continuously flowing KOH 1 mM solution on the quartz crystal surface, then frequency and dissipation signals were off-set to zero just before injection of dispersions in a continuous mode at a flow rate of 100 µL min^{-1}. t-CNC and t-CNC-Gx dispersions (0.3 g L^{-1} in KOH 1 mM) and PAMAM G3 solution (0.001 g L^{-1} in KOH 1 mM) were injected into the QCM-D cell until a plateau value of frequency and dissipation signals was reached. Then, a rinsing step of the surface with KOH 1 mM was performed. For the study of the pH-response, after the adsorption of t-CNC-Gx on the gold surface followed by the rinsing step, the pH was cycled between pH 11 and pH 2 by the successive injection of aqueous solutions of KOH 1mM and HCl 10 mM, respectively. QCM-D experiments were repeated at least twice and average results of two measurements are given.

Frequency ($\Delta f_n/n$) and dissipation (ΔD_n) changes were simultaneously registered at 5 MHz fundamental resonance frequency and its several overtones as a function of time. Any material adsorbed on the crystal surface induces a decrease of the resonance frequency $\Delta f_n/n$. Dissipation signals (ΔD_n) were recorded simultaneously to frequency shifts and they provided a measure of the frictional losses due to the viscoelastic properties of the adsorbed layer. The overtone n = 5 was used for comparing the adsorption of unmodified and modified t-CNCs. If the adsorbed mass is evenly distributed, rigidly attached and small compared to the mass of the crystal, $\Delta f_n/n$ is directly proportional to the adsorbed mass per surface unit (Γ) using the Sauerbrey's equation (Sauerbrey, 1959) :

$$\Gamma_{QCM} = -C \frac{\Delta f_n}{n} \qquad \text{(Equation 1)}$$

where C is the constant for the mass sensitivity of the quartz crystal (0.177 mg m^{-2} Hz^{-1} at f_0 = 5 MHz) and n is the overtone number.

Sauerbrey's equation was used to estimate the deposited mass of t-CNC-Gx on the gold surface. Indeed, the very low values of ΔD_n recorded combined to almost no separation of all overtones signals (Fig. S2 to S5) suggested the formation of rigid layers on the gold surface, and validated the use of the Sauerbrey's equation.

2.3.4. Surface Plasmon Resonance (SPR)

The SPR measurements were performed with a Biacore x100 (GE Healthcare, Sweden) using gold substrates. All measurements were carried out at 20 °C with a 0.3 g L^{-1} suspension in KOH 1mM at 10 µL min^{-1}. Results are expressed as the mean of two experiments. Molecules adsorbing on the surface change the solute and solvent concentration profiles and thus the refractive index within the evanescent wave range, and the resonance angle increases ($\Delta\theta$). From this angle, one can calculate the adsorbed mass per surface unit using the following equation (Orelma, Filpponen, Johansson, Laine, & Rojas, 2011; Tulpar & Ducker, 2004; Wintgens & Amiel, 2005):

$$\Gamma_{SPR} = \frac{l_d}{2} \cdot \frac{\Delta\theta}{m\left(\frac{dn}{dc}\right)} \qquad \text{(Equation 2)}$$

Where l_d is the decay length of the evanescent electromagnetic field estimated as 0.37 of the light wavelength (λ_d = 760 nm), m is the calibration coefficient of the sensor (m = 103.3°) and the refractive index increment, dn/dc, is 0.15 mL g^{-1} for polysaccharides in water (Potthast et al., 2015).

3. RESULTS AND DISCUSSION

3.1. Introduction of PAMAM dendrimers at reducing end of cellulose nanocrystals.

In this work, we focused on tunicate cellulose nanocrystals (t-CNC) as model nanorods because of their high aspect ratio and rather homogeneous length distribution (Habibi et al., 2010). Moreover, in contrast to cotton or wood CNCs, nanocrystals from tunicate are composed of a single crystal displaying parallel arrangement of cellulose chains, which is of interest when aiming to functionalize the reducing end. t-CNCs appeared as long rod-like nanocrystals, with an average length of 1360±630 nm and an average width of 11±3 nm (Villares et al., 2018). They were well individualized in water and there was no evidence of large-scale aggregation, as previously described (Sacui et al., 2014; Zhao, Zhang, Lindström, & Li, 2015). The colloidal suspension was stable in water because t-CNCs were negatively charged due to the sulfate groups introduced during acid hydrolysis as confirmed by their value of zeta potential around -27 mV.

t-CNCs were asymmetrically functionalized by introducing poly(amidoamine) dendrimers (PAMAM) at their reducing ends. PAMAMs of 4 generations were compared, from a very small molecule (G0) to a globular dendrimer (G3) as shown in Fig. 1. They had an ethylenediamine core and multiple amine groups at their surface, whose number increases exponentially with the PAMAM generation. Dendrimers structural parameters are summed up in Table S1.

The reactivity of PAMAM amine groups was used for coupling them to the oxidized reducing ends of t-CNCs by amide bonds as illustrated in Fig. 2. Thus, at first, aldehyde groups of t-CNC reducing ends were oxidized to carboxylic acid groups and, then, the PAMAM amine groups

reacted with the NHS/EDC activated carboxylic acid groups. Arcot *et al.* have also used this strategy to introduce thiol moieties at the reducing ends of CNCs by using 6-amino-1-hexanethiol. They showed that this method is a mild way for the synthesis of asymmetric CNCs preventing their aggregation during the reaction in contrast to reductive amination (Arcot et al., 2014). Unspecific adsorption of PAMAMs onto the t-CNC surface was limited since the reaction was carried out in a high ionic strength media (0.3 M) and at basic pH over 9.2 to screen the electrostatic interactions between the sulfate groups of t-CNCs and the amine groups of PAMAMs.

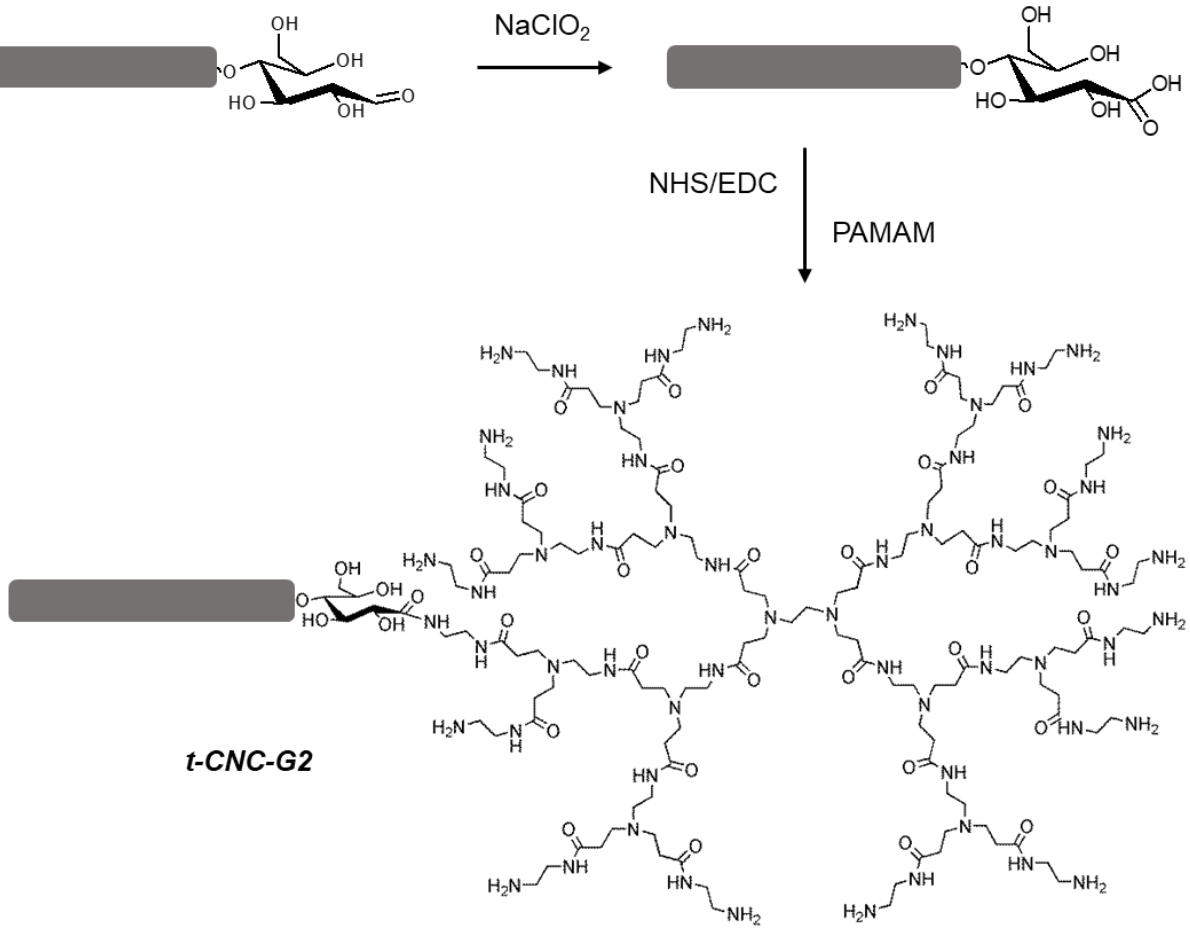

Fig. 2. Schematic illustration of the synthetic protocol used to graft PAMAM G2 at the reducing end of t-CNC, involving a first step of oxidation and a second step of carbodiimide coupling. Dimensions of t-CNC (grey rectangles) and chemical structures are not at scale.

By specifically functionalizing the t-CNC reducing end, the number of PAMAM functional groups is small compared to the number of glucose units in the cellulose nanocrystal, and common techniques such as elementary analysis or infrared spectroscopy are not sensible enough to detect the introduction of PAMAM functionalities (Kaldéus, Nordenström, Carlmark, Wågberg, & Malmström, 2018; Villares et al., 2018; Zoppe et al., 2017). In a recent study, Heise *et al.* employed advanced liquid-state NMR techniques to characterize CNCs after the introduction of a β-diketon functionality at their reducing end (Heise et al., 2019). Nevertheless, the detection of the reducing end modification required complete dissolution of CNCs in ionic liquids to facilitate NMR signal resolution. This study demonstrated that the elucidation of the chemical structure, and therefore, the detection of functionalities at the reducing ends of cellulose nanocrystals is a real analytical challenge to consider. In our work, we demonstrated the introduction of PAMAM functionalities at the reducing ends of t-CNCs by studying the suspension stability and the behavior of the nanocrystals before and after PAMAM functionalization in contact to gold surfaces as indirect proofs of successful PAMAM hybridation.

3.2. Stability of PAMAM functionalized t-CNC suspensions

Regardless of pH, t-CNCs are negatively charged due to sulfate groups present on their surface. Differently, the charge of PAMAMs is pH dependent since both primary and tertiary amine groups are assumed to be unprotonated above pH 10 whereas they are fully protonated below pH 4, and therefore, positively charged (Lee et al., 2002). In pure water, PAMAMs are then

partially positively charged and may interact with negatively charged t-CNCs leading to aggregation (L. Chen et al., 2015). Therefore, to stabilize the suspension, it may be interesting to work at basic pH to ensure the PAMAM neutrality. Indeed, the stability of the colloidal suspensions of t-CNC-Gx was investigated in pure water and in KOH 1 mM (pH 11) by zeta potential measurements and dynamic light scattering (DLS). DLS measures the diffusion of nanoparticles due to the Brownian motion and thus the rate at which the intensity of scattered light fluctuates in time is monitored. Then, the correlation function of the scattered intensity is used to illustrate the sample state in terms of mean size, dispersion and aggregation state. Indeed, scattered signal of aggregates fluctuates slower than dispersed particles, and the suspensions can be characterized by plotting the autocorrelation function as a function of time (correlogram). Then, longer delay times indicate larger particles and a steeper slope indicates a more monodisperse sample. Thus, comparison of the correlograms is a qualitative mean to compare the aggregation state of the different modified nanorods. The zeta potentials (*pZ*) and the corresponding correlograms of t-CNC-Gx suspensions, as well as photographs of t-CNC-G2 suspensions, either in water or in KOH 1mM are displayed in Fig. 3. Photographs of the four t-CNC-Gx suspensions either in water or in KOH 1mM are displayed in Fig. S1.

A	*pZ* (mV)
t-CNC	-27.4 ± 2.5
t-CNC-G0	-16.5 ± 0.8
t-CNC-G1	-18.2 ± 1.0
t-CNC-G2	15.1 ± 1.0
t-CNC-G3	32.1 ± 0.7

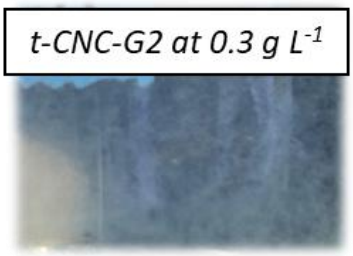

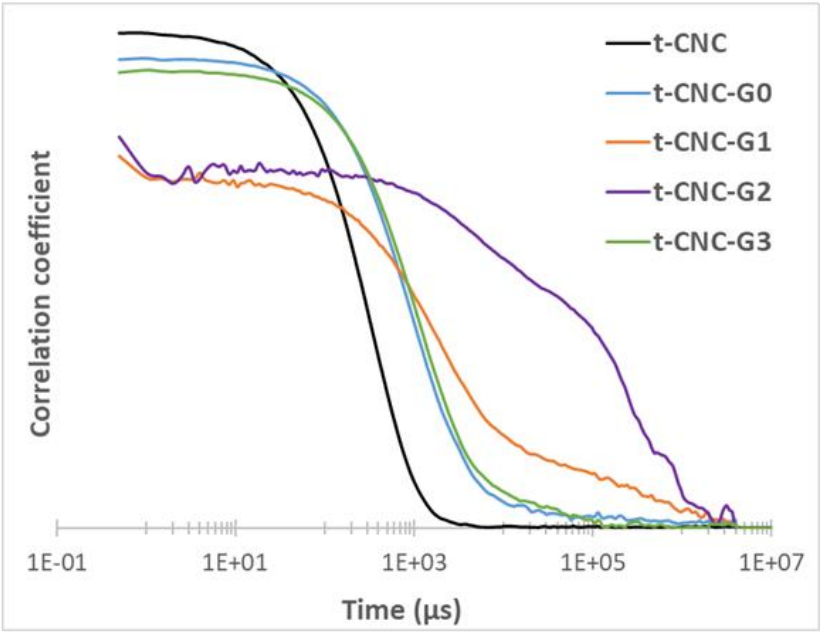

B	*pZ* (mV)
t-CNC	-26.8 ± 2.1
t-CNC-G0	-30.4 ± 1.0
t-CNC-G1	-31.8 ± 1.3
t-CNC-G2	-29.0 ± 1.2
t-CNC-G3	-22.9 ± 1.8

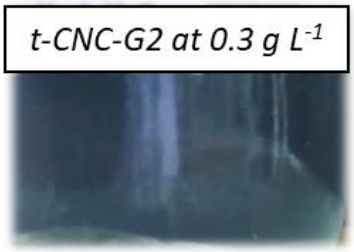

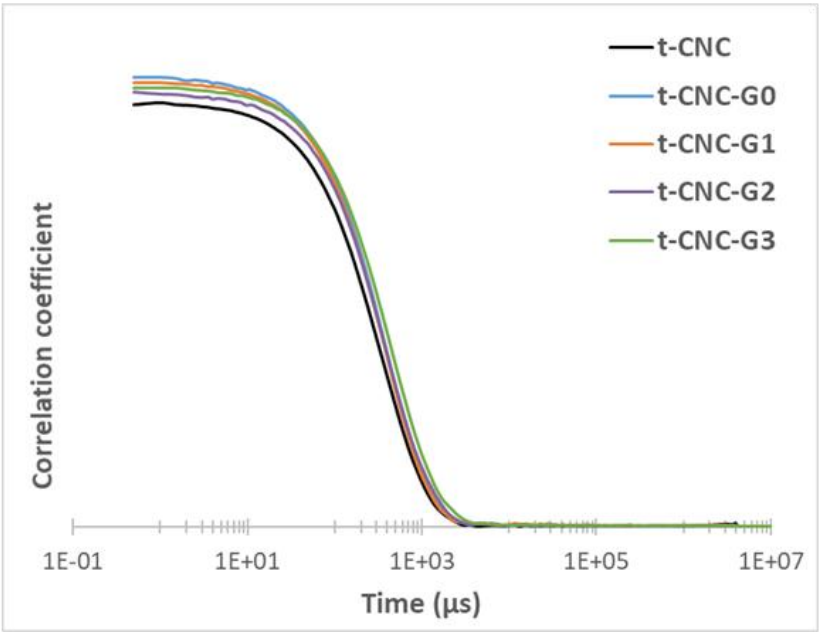

Fig. 3. Zeta potential (*pZ*) values and DLS correlograms for t-CNCs before and after PAMAM functionalization at 0.1 g L^{-1} in A. water and B. KOH 1 mM. Additionally photographs of tubes containing t-CNC-G2 suspensions at 0.3 g L^{-1} in A. water and B. KOH 1mM are shown.

In the case of t-CNC and t-CNC-Gx in pure water (Fig. 3A), the introduction of PAMAM at the reducing end produced a remarkable effect on correlation coefficients. Correlograms showed

three different aggregation states. The far most aggregated sample was t-CNC-G2 followed by the t-CNC-G1 hybrids, which were significantly more aggregated than t-CNC-G0 and t-CNC-G3. Thus, the aggregation is likely due to the interaction between positively charged amine groups of PAMAMs and the negatively charged t-CNCs. Therefore, the aggregation state depends on the PAMAM generation, which determines the number of amine groups and therefore the balance between negative and positive charges. In order to give more insight into the charge balance, the zeta potential of the t-CNC-Gx suspensions was determined. *pZ* provides an indirect measurement of the "net charges" on the aggregated particles surface by measuring the zeta potential at the interface between the electrical double layer of particles and water. For t-CNC-G0 and t-CNC-G3, the lower extent of aggregation can be justified by the charge imbalance. Thus, in the case of t-CNC-G0, the number of amine groups from PAMAMs is so small that the sulfate groups from t-CNCs ensure the suspension stabilization. This assumption was demonstrated by the negative values of zeta potential. Differently, for t-CNC-G3, the positive values of zeta potential suggested that the number of amine groups from PAMAMs is high compared to the number of sulfate groups from t-CNCs, which ensures colloidal stabilization by the positive charges. In the case of t-CNC-G1 and t-CNC-G2 there was a drastic change towards a more pronounced aggregation state, as illustrated on the photograph of the t-CNC-G2 suspension in water (Fig. 3A). A fair hypothesis would be that PAMAMs G1 and G2 had an intermediate charge density whose value promotes a significant aggregation through electrostatic interactions. Moreover, some of the PAMAM charges could be screened inside the aggregates, which explains a non-linear increase of pZ values with PAMAM generation.

To ensure that these aggregation states were due to charged PAMAMs, we then studied the suspensions of t-CNC and t-CNC-Gx in KOH 1 mM at 0.1 g L^{-1} (Fig. 3B). At pH 11 amine groups from PAMAMs are not charged and no electrostatic attraction would occur between PAMAMs and t-CNCs. The correlograms of all t-CNC-Gx were very similar to the one of unmodified t-CNC, which confirmed that hybrid nanoparticles were well-dispersed in KOH 1 mM (no aggregation) as seen on the photograph of the t-CNC-G2 suspension in KOH 1 mM (Fig. 3B). The *pZ* values of all suspensions were then close to the one of unmodified t-CNCs confirming that amino groups were not protonated. The t-CNC-Gx suspensions were therefore stabilized by electrostatic repulsions between nanocrystals, as shown by the visual examination of the suspensions (photographs on Fig. S1). The individualization of t-CNC-Gx in KOH 1 mM was confirmed by scanning transmission electron microscopy (STEM). Representative images of every t-CNC-Gx suspension either in pure water or in KOH 1 mM are presented on Fig. S2. The morphology comparison between t-CNC before and after PAMAM coupling confirmed first that t-CNC-Gx were well dispersed in KOH 1 mM and then that the PAMAM functionalization did not affect the t-CNC morphology. Representative STEM images of hybrid t-CNC-PAMAM (t-CNC-G2) compared to native t-CNC in KOH 1 mM are shown in Fig. 4. Chen *et al.* introduced PAMAM dendrimers at the surface of CNCs and showed that their suspensions was stable either at acidic or basic pH (L. Chen et al., 2015). In our case, it is interesting to notice that despite the very small amount of introduced amine groups at the nanocrystal end, the aggregation state depends on pH. Therefore, we decided to work in KOH 1 mM to have individualized hybrid CNC-PAMAM particles and to study their adsorption behavior on gold surface. This aqueous solvent have the advantage to be fully compatible with QCM-D and SPR measurements.

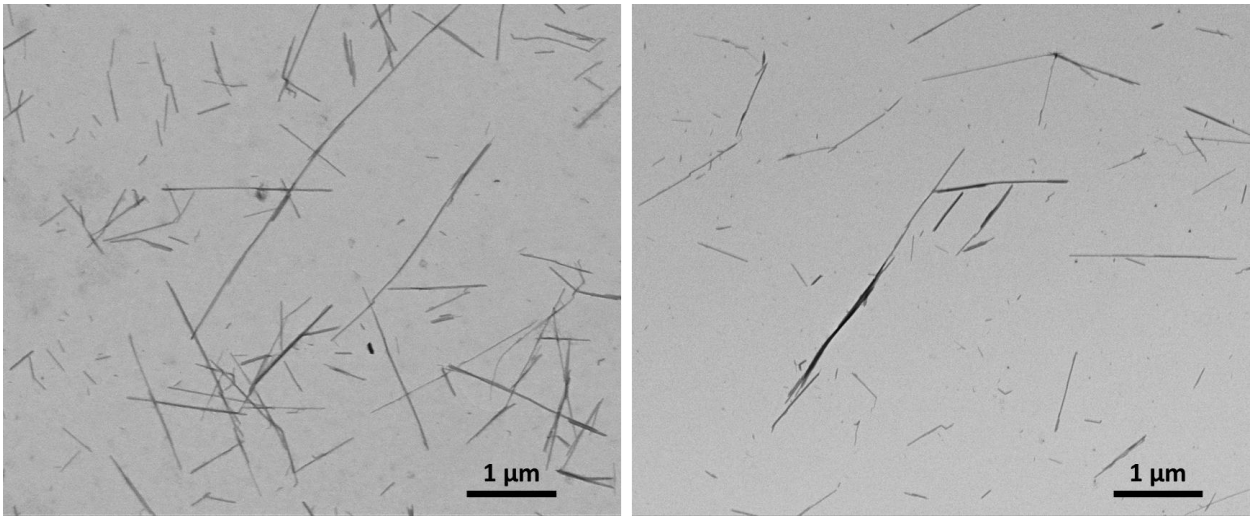

Fig. 4. Representative STEM images of native t-CNC (left) and t-CNC-G2 (right) at 0.2 g L^{-1} in KOH 1 mM

3.3. Adsorption of PAMAM functionalized t-CNCs on gold surface

The affinity of amine groups for gold was used to adsorb t-CNC-Gx on gold surface. Their adsorption behavior was investigated by quartz crystal microbalance with dissipation (QCM-D) and surface plasmon resonance (SPR). The objective of this set of experiments was to demonstrate the selective binding of PAMAM functionalized t-CNCs on gold and to further study their adsorption behavior. Moreover, the comparison between QCM-D and SPR allows the calculation of the amount of water trapped in the deposited layer (Eronen, Junka, Laine, & Österberg, 2011; Hedin, Löfroth, & Nydén, 2007; C. Wang et al., 2012).

Firstly, t-CNC-Gx suspensions in KOH 1 mM were studied by QCM-D and the changes in frequency and dissipation were monitored upon time (Fig. 5). The changes of $\Delta f_n/n$ and ΔD_n signals for overtone numbers n = 3, 5, 7, 9, 11 and 13 for t-CNC-G0, t-CNC-G1, t-CNC-G2 and t-CNC-G3 upon time are depicted on Fig. S3, S4, S5 and S6, respectively.

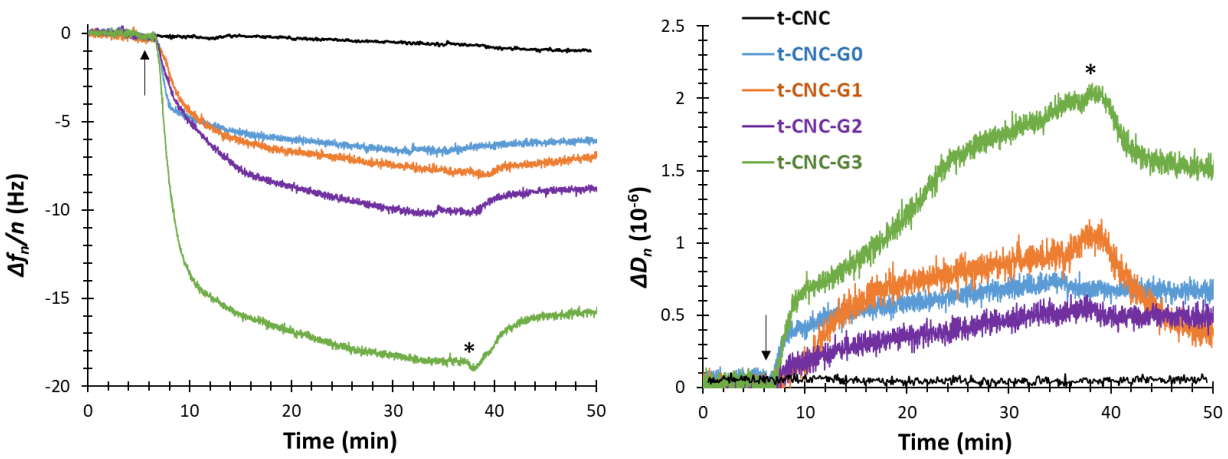

Fig. 5. Frequency ($\Delta f_n/n$) and dissipation (ΔD_n) changes for the overtone n = 5 monitored by QCM-D during adsorption of t-CNC and t-CNC-Gx (x = 0, 1, 2, 3) at 0.3 g L^{-1} in KOH 1 mM. The arrow indicates the injection of t-CNCs and the asterisk the rinsing step with KOH 1 mM.

When t-CNC-Gx were injected, changes in frequency and dissipation were observed, indicating adsorption onto the gold surface. Since unmodified tunicate nanocrystals did not adsorbed onto gold substrates due to the repulsion between the anionic sulfate groups and the negatively charged gold surfaces (black line on Fig. 5), then the adsorption of t-CNC-Gx was due to PAMAM amine moieties. The irreversibility of the binding was assessed by rinsing with KOH 1 mM, which did not induce significant changes nor in frequency nor in dissipation. QCM-D results showed that the frequency decrease and dissipation increase values are in agreement with Arcot *et al.* who described the chemisorption of CNCs on gold by their thiol-functionalized reducing end (Arcot et al., 2014, 2013). Moreover, the changes observed with t-CNC-Gx adsorption increased with PAMAM generation. More specifically, a gap was observed between generations G2 and G3. For x = 0, 1, 2, the changes in frequency were very close, between -6 and -9 Hz, as well as the changes in dissipation between 0.4×10^{-6} and 0.7×10^{-6}, while for generation x = 3 the changes in frequency and dissipation were much higher, about -16 Hz and $1.5.10^{-6}$ respectively. This non-linearity in frequency and dissipation changes may not only

361 suggest a higher adsorbed mass for t-CNC-G3 but also a difference in the adsorption process.
362 The very low dissipation values obtained for x = 0, 1 and 2 may also indicate that the amount of
363 adsorbed nanoparticles is too low for completely covering the gold surface. For t-CNC-G3, the
364 amount of adsorbed nanoparticles may be high enough to form a continuous layer that would
365 lead to the increase in dissipation change, in line with the slight separation of overtones for
366 dissipation signals observed only for t-CNC-G3 (Fig. S3 to S6).
367 Deeper QCM-D results analysis can lead to the determination of the kinetic constant of the
368 adsorption process. In a previous study (Chemin, Moreau, Cathala, & Villares, 2020), we
369 detailed a kinetic modeling to determine kinetic constants based on the collision between a
370 particle and a surface (supplementary material), which is valid independently of the particles
371 content in the system (Alince, Petlicki, & van de Ven, 1991). Briefly, the frequency values
372 obtained by QCM-D were transformed onto surface coverage by using the Sauerbrey's
373 expression (Equation 1 in section 2.3.3.). The experimental fractional coverage values as a
374 function of time are then plotted as shown in Fig. 6. The fit of these data allowed the
375 calculation of the apparent kinetic constant given by $\alpha_0 k_{12} S$ where α_0 is the collision rate
376 efficiency factor, k_{12} is the rate constant and S is the initial number of surfaces per unit volume.
377 Plots on Fig. 6 showed a good fit between the theoretical prediction (Equation S3) and the
378 measured data for all the t-CNC-Gx studied. Values obtained for the kinetic constant $\alpha_0 k_{12} S$
379 confirmed a different adsorption behavior between the three first t-CNC-Gx (x = 0, 1, 2) and t-
380 CNC-G3 with a drastic change in the kinetic constant increasing from $0.6/0.8.10^{-3}$ min^{-1} to
381 $2.4.10^{-3}$ min^{-1} (Fig. 6). PAMAM G3 is the biggest globular dendrimer used that has 32 amino
382 groups with most of them accessible to adsorb on the gold surface, so that the collision rate

efficiency factor may be higher. QCM-D results showed a breaking point in the adsorption behavior that occurred between t-CNC-G2 and t-CNC-G3. Results suggested that PAMAM G3 had a critical size, which marked a change in properties.

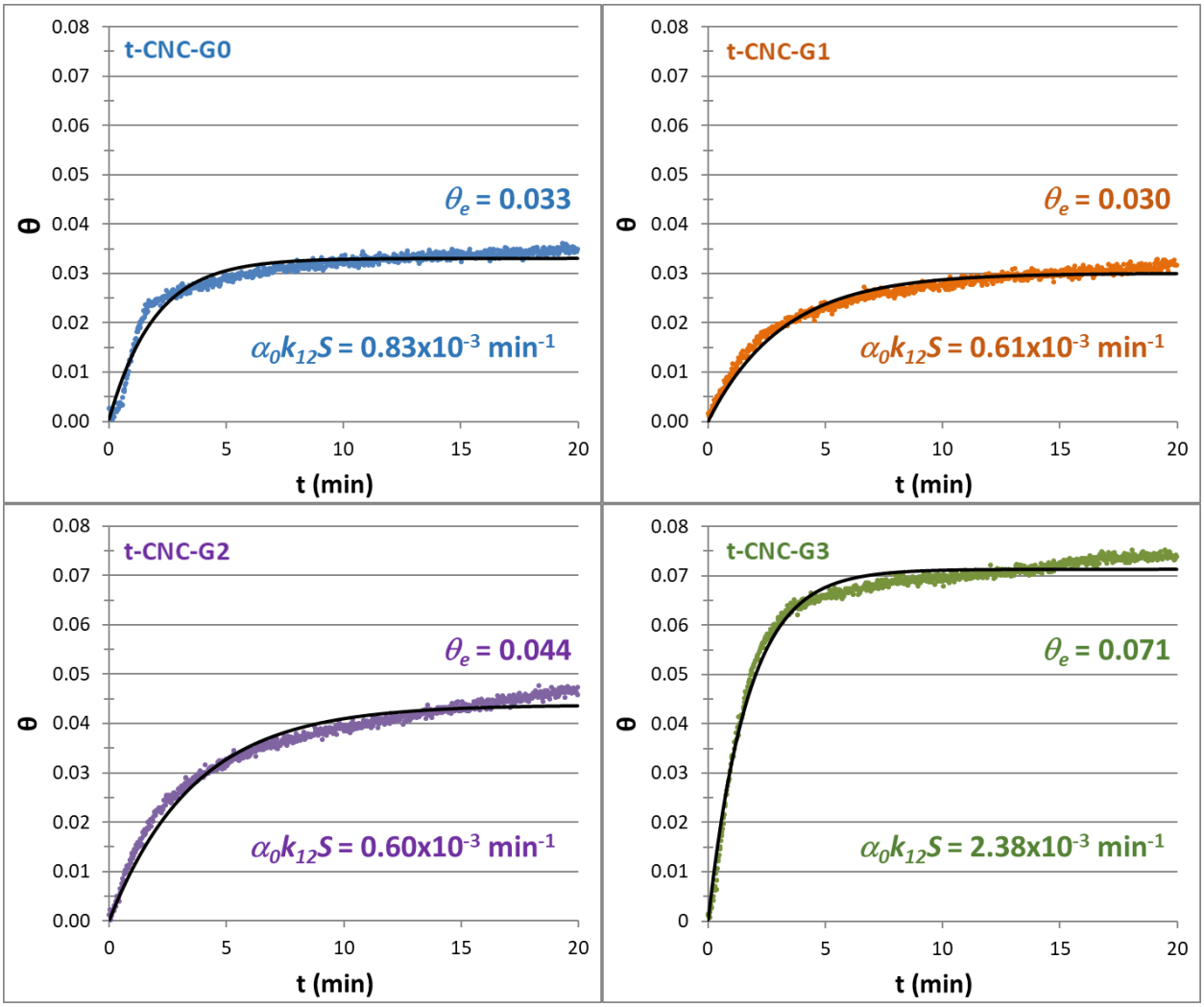

Fig. 6. Fractional surface coverage for t-CNC-Gx as a function of time. The colored dots correspond to experimental data fitted by the Sauerbrey model and the solid black lines represent the fit to Equation S3, allowing the calculation of the apparent kinetic constant $\alpha_0 k_{12} S$ and the equilibrium fractional surface coverage θ_e.

In an attempt to obtain more insight into the adsorption process of t-CNC-Gx, their adsorption onto gold surfaces was then studied by SPR. The SPR technique is based on the resonant

oscillation of electrons occurring at the interface between a conductive metal and dielectric fluid when stimulated by incident light. As these oscillations are very sensitive to any change at the interface, the adsorption of molecules onto the conducting surface can be monitored. The mechanism of detection is based on changes in the local index of refraction by the adsorbing molecules, changing the resonance conditions of the surface plasmon waves and the angle of minimum reflection ($\Delta\theta$) (Ahola, Myllytie, Österberg, Teerinen, & Laine, 2008). The angle shift was then monitored upon time (Fig. 7) and allowed to calculate the deposited mass according to calculations detailed in the experimental section (Equation 2 in section 2.3.4.). The adsorption of t-CNC-Gx monitored by SPR gave similar trends than QCM-D, the amount of adsorbed t-CNC-Gx increased with PAMAM generation. The same gap was observed between generations G2 and G3 with a much higher adsorbed mass of 88 ng cm^{-2} on gold surface for t-CNC-G3. For a molecular layer, the shift in the SPR angle is usually referred as the "optical thickness" and does not take the water mass into account (Schoch & Lim, 2013). Therefore, combining SPR and QCM experiments, the amount of trapped water in the adsorbed layer can then be calculated as (C. Wang et al., 2012) (see results in Fig. 7) :

$$\%\ \text{water} = \left[1 - \left(\frac{\Gamma_{SPR}}{\Gamma_{QCM}}\right)\right] \times 100 \qquad \text{(Equation 3)}$$

For all t-CNC-Gx, the amount of trapped water was high, between 68% and 87%. The lowest water amount was obtained with t-CNC-G3. In fact, the SPR results indicated that the mass adsorption of t-CNC-G3 was 6 times higher than t-CNC-G0, and 3 times higher than t-CNC-G1 and t-CNC-G2. The increase in PAMAM generation seemed to favor the adsorption of PAMAM-functionalized t-CNC, and a higher number of hybrid t-CNC were adsorbed onto the gold

surface. This fact could be justified by the increasing number of anchoring groups, so the interaction of the amino groups with the gold surface could result in a rather flat conformation of PAMAM, which may favor water expulsion.

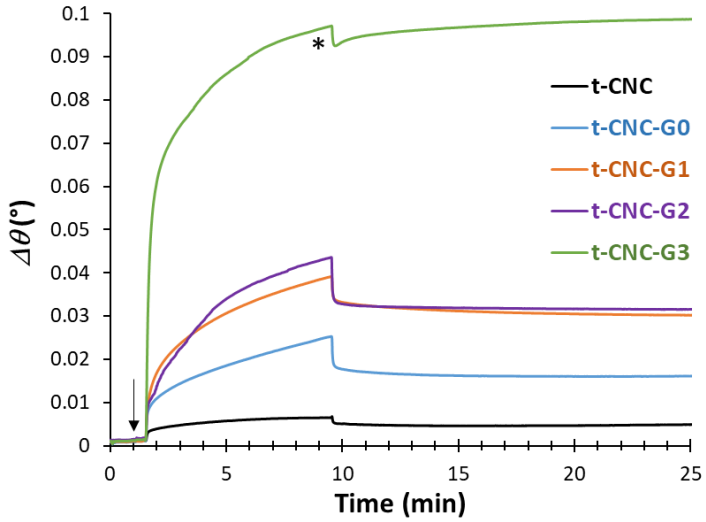

	Γ_{SPR} (ng cm^{-2})	Γ_{QCM} (ng cm^{-2})	% water
t-CNC-G0	13.7	105.2	87.0
t-CNC-G1	26.5	117.6	77.5
t-CNC-G2	27.1	154.6	82.5
t-CNC-G3	88.4	276.4	68.0

Fig. 7. Angle changes ($\Delta\theta$) monitored by SPR during adsorption of t-CNC and t-CNC-Gx (x = 0, 1, 2, 3) at 0.3 g L^{-1} in KOH 1 mM. The arrow indicates the injection and asterisk the rinsing step; and the respective calculated masses adsorbed using SPR and QCM experiments to obtain the amount of trapped water

3.4. Viscoelastic properties of t-CNC-Gx adsorbed on gold surfaces

QCM-D allows investigating the arrangement of hybrid t-CNCs onto the solid surfaces as well as the properties of the adsorbed layers. For that purpose, the changes in ΔD_n were plotted as a function of $\Delta f_n/n$ (Fig. 8). The slope of the ΔD_n *vs* $\Delta f_n/n$ plot reveals at any point of the curve how much dissipation is induced by frequency unit allowing a comparison of the viscoelasticity characteristics of the deposited layers (Ahola, Salmi, Johansson, Laine, & Österberg, 2008; Rodahl et al., 1997). Thus, the absolute slope and changes in the slope in the plots provide information about the adsorption regimes and conformation changes (Amirkhani, Volden, Zhu, Glomm, & Nyström, 2008).

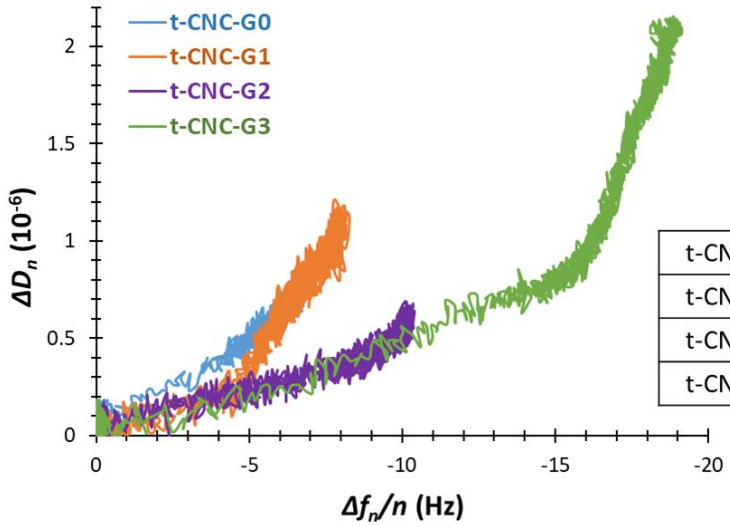

	Slope of adsorption step x 10^{-6} Hz^{-1}	Slope of equilibration step x 10^{-6} Hz^{-1}
t-CNC-G0	0.07	0.14
t-CNC-G1	0.05	0.23
t-CNC-G2	0.04	0.13
t-CNC-G3	0.05	0.41

Fig. 8. Change in dissipation as a function of the change in frequency (ΔD_n - $\Delta f_n/n$) for the overtone n = 5 corresponding to t-CNC-Gx at 0.3 g L^{-1} in KOH 1 mM adsorbed onto gold surfaces; and the respective calculated slopes (x 10^{-6} Hz^{-1})

For the adsorption of t-CNC-Gx on gold, ΔD_n increased linearly with increasing frequency but two different slopes occurred, which suggested that nanocrystals did undergo orientation changes in the course of the adsorption process (Amirkhani et al., 2008). After the adsorption step - which exhibit a very small slope between 0.04x10^{-6} and 0.07x10^{-6} Hz^{-1} according to the ΔD_n - $\Delta f_n/n$ plot - occurred an equilibration step having a higher slope. For the three first hybrids having the PAMAM from G0 to G2, the slope of the equilibrium step was between 0.13x10^{-6} and 0.23x10^{-6} Hz^{-1}. The obtained values were in agreement with the work of Arcot *et al.*, which described the chemisorption of thiol-functionalized CNCs in an upright orientation by the increase in the ΔD_n - $\Delta f_n/n$ slope compared to the adsorption in a flat orientation (Arcot et al., 2013). The increase of the ΔD_n - $\Delta f_n/n$ slope up to 0.41x10^{-6} Hz^{-1} was then more marked in the case of t-CNC-G3. PAMAM G3 is the largest dendrimer studied, and the size and flexibility of poly(amidoamine) branches could provide enough freedom to the hybrid nanorods to straighten. Therefore, hybrid t-CNCs would bond to the gold surface in a rather upright

orientation with the non-reducing end facing up. In order to support this hypothesis, the adsorption of PAMAM G3 dendrimer on gold was also monitored by QCM-D and the changes in ΔD_n were plotted as a function of $\Delta f_n/n$ (Fig. 9). The adsorption behavior of PAMAM G3 was very different compared to t-CNC-G3. Two regimes were also observed but the slope of the equilibration step (0.03×10^{-6} Hz^{-1}) was smaller than the one of the adsorption step (0.10×10^{-6} Hz^{-1}). During adsorption, the ΔD_n - $\Delta f_n/n$ slope of PAMAM G3 was slightly higher than the slope of t-CNC-G3 because nanocrystals may have a stiffening effect. After the adsorption, the decrease of the slope for PAMAM G3 indicated a conformation change that may induce a thinner and/or more rigid layer (X. Wang, Ruengruglikit, Wang, & Huang, 2007; Zhou et al., 2004). PAMAM dendrimers may maximize their interactions with the surface leading to a flattening effect. Indeed, Mecke *et al.* studied the deformation of PAMAMs from G2 to G5 on mica surfaces and showed that flattening of dendrimers occurred at the liquid-solid interface with multiple interaction sites between the branched ends and the substrate (Mecke, Lee, Baker, Holl, & Orr, 2004). These data could explain that the increase of the slopes during the equilibrium step of t-CNC-Gx adsorption was due to the cellulose nanorods, which must reorganize as a hairy layer. Indeed, hybrid t-CNCs benefited enough freedom thanks to PAMAM dendrimer as attachment point to adopt an upright orientation and repelled each other electrostatically due to the presence of sulfate groups along the nanocrystal surface. This phenomenon was more noticeable in the case of t-CNC-G3 thanks to the higher PAMAM size and flexibility.

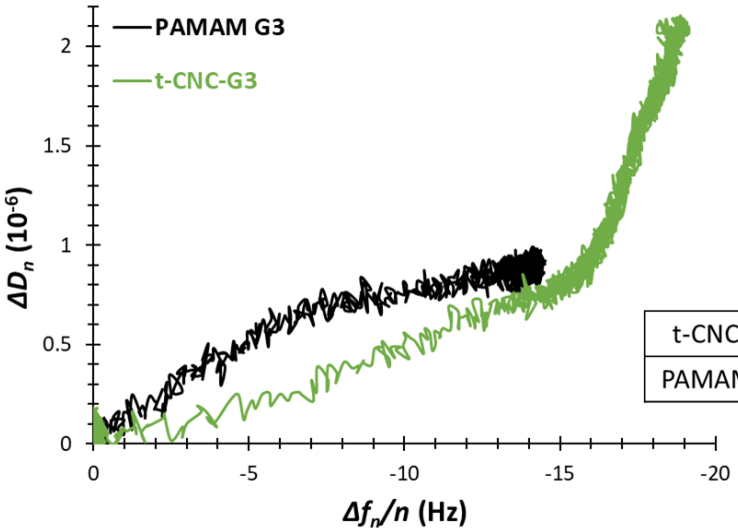

	Slope of adsorption step x 10^{-6} Hz^{-1}	Slope of equilibration step x 10^{-6} Hz^{-1}
t-CNC-G3	0.05	0.41
PAMAM G3	0.10	0.03

Fig. 9. Change in dissipation as a function of the change in frequency (ΔD_n - $\Delta f_n/n$) for the overtone n = 5 corresponding to t-CNC-G3 at 0.3 g L^{-1} in KOH 1 mM (green) and to PAMAM G3 at 0.001 g L^{-1} in KOH 1 mM (black) adsorbed onto gold surfaces; and the respective calculated slopes (x 10^{-6} Hz^{-1}) which are indicated with dashed lines.

3.5. pH response of t-CNC-Gx adsorbed layers on gold surfaces

One of the particularities of anchoring PAMAM at the reducing end of t-CNC was the introduction of multiple amine groups that are sensitive to pH. The protonation of the amine groups at low pH leads to electrostatic repulsions between charged groups and their subsequent separation, which results in water uptake. The swelling behavior of t-CNC-Gx layers at different pHs was investigated by QCM-D as is was shown to inform about polymers conformational modifications upon pH changes (Howard, Craig, Fitzgerald, & Wanless, 2010). After the adsorption of t-CNC-Gx as previously described, four solvent exchange – from KOH 1 mM to HCl 10 mM – were performed and the changes in frequency and dissipation were recorded (Fig. 10).

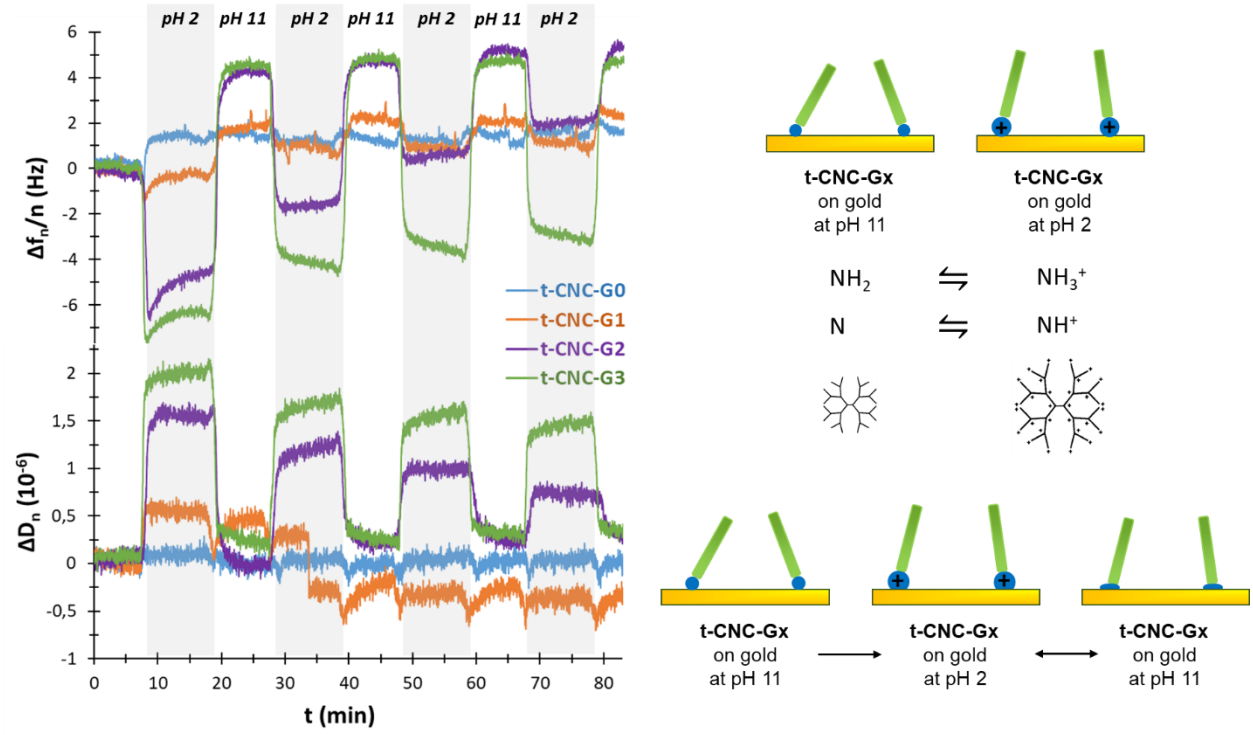

Fig. 10. Change in frequency and in dissipation as a function of time for the overtone n = 5 corresponding to t-CNC-Gx adsorbed on gold surfaces, submitted to solvent exchange from KOH 1 mM to HCl 10 mM (4 consecutive times) showing swelling as illustrated on the right.

In the case of t-CNC-G0, the grafted PAMAM G0 was too small to clearly respond to pH changes. Both frequency and dissipation showed only slight variations. Differently, starting from PAMAM G1 the response to pH increased with the PAMAM generation. When the solvent was changed from alkaline to acidic pH, from KOH 1 mM to HCl 10 mM respectively, a spectacular decrease in frequency concomitant to an increase in dissipation occurred, which was consistent with swelling. Indeed, PAMAM move from a globular and loosely compact structure at pH 11 to an highly extended one at pH 2 with amine groups protonation and water uptake (Lee et al., 2002). This was confirmed by the separation of the overtones only at pH 2 (t-CNC-G3 on Fig. S7) showing a more viscoelastic behavior thanks to swelling. When the pH was changed back to alkaline, an increase in frequency concomitant to a decrease in dissipation

occurred, showing reversibility, and the swelling and the deswelling processes occurred at similar rate. Comparing t-CNC-G2 and t-CNC-G3, it is very interesting to note that their $\Delta f_n/n$ and ΔD_n values in KOH 1 mM were similar while they differed in HCl 10 mM. This phenomenon corroborated the Lee's et al. study, who explained using computer simulations that at high pH, the atom density distribution is conserved across generations while at low pH, the interior hollow spaces of PAMAM increased with generation grows (Lee et al., 2002).

After the first solvent exchange, it seemed that even more water was expelled from the layer since during the second cycle in KOH 1 mM, the frequency plateau value was higher than at the beginning of the experiment. The changes in ΔD_n were plotted as a function of $\Delta f_n/n$ for each solvent exchange (Fig. S8). Interestingly, these plots revealed that the first solvent exchange (orange dots on Fig. S8) was shifted from all the others (gray dots on Fig. S8), showing that the first change in conformation was non-reversible. The swelling occurring in HCl 10 mM must increase the PAMAM area in contact with the gold surface, and therefore the interactions between charged amine moieties of PAMAM and gold increased. These new interactions may be strong enough to resist to the next solvent exchange. Back in KOH 1 mM, the PAMAM deswelling may then lead to a flatter and more rigid PAMAM anchoring as illustrated on Fig. 10, explaining the higher frequency plateau value in KOH 1 mM for the following cycles. The reversibility of this phenomenon was evaluated by repeating cycles between alkaline and acidic pH several times. After the first solvent exchange, this phenomenon is remarkably reversible and reproducible (within instrumental drift) but the intensity of the t-CNC-Gx response to pH was decreased. There might be a reinforcement of the PAMAM interactions with gold during

multiple cycles explaining the decreasing PAMAM response to pH. The PAMAM generation used could then allow tuning the pH response of these functional materials.

4. CONCLUSION

In this work, bio-based materials were obtained by grafting PAMAM dendrimers at the reducing end of tunicate cellulose nanocrystals in mild conditions. These hybrid asymmetric nanoparticles showed that the PAMAM functionalities led to a reducing end-driven adsorption on gold. We succeeded in the formation of hairy layers combining the properties of rigid rod-like nanocrystals to globular and flexible PAMAM dendrimers. Multiple solvent exchange from pH 11 to pH 2 showed a remarkable reversible response to pH of these functional materials. The size of the PAMAM dendrimer determined the arrangement of the adsorbed layer, and the change from PAMAM G2 to PAMAM G3 clearly modified the adsorbed mass, water content and pH-responsive properties.

This work may bring new opportunities for the development of pH-responsive hairy surfaces, since it demonstrates that properties can be tuned by changing the PAMAM generation.

APPENDIX. Supplementary Material

Author Contributions

AV and MC designed the experimental plan and conducted project development. MC completed the experimental work and data analyses. AV, BC, and CM conceived the project and

contributed to data analysis, especially the QCM-D. MC prepared the manuscript and all authors read, revised and approved the submitted version.

Funding Sources

French National Research Agency (Project Cellmach, ANR-17-CE07-0010-01)

Conflict of Interest

The authors declare that the research was conducted in the absence of any commercial or financial relationships that could be construed as a potential conflict of interest.

ACKNOWLEDGEMENTS

The authors gratefully acknowledge the French National Research Agency (Project Cellmach, ANR-17-CE07-0010-01) for financial support. We greatly thank Dr. Hervé Bizot for the preparation of tunicate nanocrystals. The authors acknowledge the BIBS platform of INRA Angers-Nantes for the access to scanning transmission electron microscopy (Dr. Bruno Novalès).

REFERENCES

Ahola, S., Myllytie, P., Österberg, M., Teerinen, T., & Laine, J. (2008). Effect of Polymer Adsorption on Cellulose Nanofibril Water Binding Capacity and Aggregation. *BioResources*, *3*(4), 1315–1328.

Ahola, S., Salmi, J., Johansson, L.-S. S., Laine, J., & Österberg, M. (2008). Model films from native cellulose nanofibrils. Preparation, swelling, and surface interactions. *Biomacromolecules*, *9*(4), 1273–1282. https://doi.org/10.1021/bm701317k

566 Alince, B., Petlicki, J., & van de Ven, T. G. M. (1991). Kinetics of colloidal particle deposition on
567 pulp fibers 1. Deposition of clay on fibers of opposite charge. *Colloids and Surfaces*, *59*,
568 265–277. https://doi.org/10.1016/0166-6622(91)80251-I
569 Amirkhani, M., Volden, S., Zhu, K., Glomm, W. R., & Nyström, B. (2008). Adsorption of cellulose
570 derivatives on flat gold surfaces and on spherical gold particles. *Journal of Colloid and*
571 *Interface Science*, *328*, 20–28. https://doi.org/10.1016/j.jcis.2008.09.013
572 Arcot, L. R., Lundahl, M., Rojas, O. J., & Laine, J. (2014). Asymmetric cellulose nanocrystals:
573 thiolation of reducing end groups via NHS–EDC coupling. *Cellulose*, *21*(6), 4209–4218.
574 https://doi.org/10.1007/s10570-014-0426-9
575 Arcot, L. R., Nykänen, A., Seitsonen, J., Johansson, L.-S. S., Campbell, J., Rojas, O. J., … Laine, J.
576 (2013). Cilia-mimetic hairy surfaces based on end-immobilized nanocellulose colloidal rods.
577 *Biomacromolecules*, *14*(8), 2807–2813. https://doi.org/10.1021/bm400633r
578 Capron, I., Rojas, O. J., & Bordes, R. (2017). Behavior of nanocelluloses at interfaces. *Current*
579 *Opinion in Colloid and Interface Science*, *29*, 83–95.
580 https://doi.org/10.1016/j.cocis.2017.04.001
581 Chemin, M., Moreau, C., Cathala, B., & Villares, A. (2020). Adsorption behavior of reducing end-
582 modified cellulose nanocrystals: a kinetic study using quartz crystal microbalance. *Journal*
583 *of Renewable Materials*, *8*(1), 29–43. https://doi.org/10.32604/jrm.2020.07850
584 Chen, L., Cao, W., Grishkewich, N., Berry, R. M., & Tam, K. C. (2015). Synthesis and
585 characterization of pH-responsive and fluorescent poly (amidoamine) dendrimer-grafted
586 cellulose nanocrystals. *Journal of Colloid and Interface Science*, *450*, 101–108.
587 https://doi.org/10.1016/j.jcis.2015.03.002

588 Chen, Li, Cao, W., Quinlan, P. J., Berry, R. M., & Tam, K. C. (2015). Sustainable Catalysts from
589 Gold-Loaded Polyamidoamine Dendrimer-Cellulose Nanocrystals. *ACS Sustainable*
590 *Chemistry and Engineering*, *3*(5), 978–985.
591 https://doi.org/10.1021/acssuschemeng.5b00110
592 Crooks, R. M., Zhao, M., Sun, L., Chechik, V., & Yeung, L. K. (2001). Dendrimer-Encapsulated
593 Metal Nanoparticles: Synthesis, Characterization, and Applications to Catalysis. *Accounts*
594 *of Chemical Research*, *34*(3), 181–190. https://doi.org/10.1021/ar000110a
595 Dadkhah Tehrani, A., & Basiryan, A. (2015). Dendronization of cellulose nanowhisker with
596 cationic hyperbranched dendritic polyamidoamine. *Carbohydrate Polymers*, *120*, 46–52.
597 https://doi.org/10.1016/j.carbpol.2014.12.004
598 Eronen, P., Junka, K., Laine, J., & Österberg, M. (2011). Interaction between water-soluble
599 polysaccharides and native nanofibrillar cellulose thin films. *BioResources*, *6*(4), 4200–
600 4217.
601 Esfand, R., & Tomalia, D. A. (2001). Poly(amidoamine) (PAMAM) dendrimers: from biomimicry
602 to drug delivery and biomedical applications. *Drug Discovery Today*, *6*(8), 427–436.
603 https://doi.org/10.1016/S1359-6446(01)01757-3
604 Favier, V., Chanzy, H., & Cavaillé, J. Y. (1995). Polymer Nanocomposites Reinforced by Cellulose
605 Whiskers. *Macromolecules*, *28*(18), 6365–6367. https://doi.org/10.1021/ma00122a053
606 Habibi, Y., Lucia, L. A., & Rojas, O. J. (2010). Cellulose Nanocrystals: Chemistry, Self-Assembly,
607 and Applications. *Chemical Reviews*, *110*(6), 3479–3500.
608 https://doi.org/10.1021/cr900339w
609 Hedin, J., Löfroth, J., & Nydén, M. (2007). Adsorption Behavior and Cross-Linking of EHEC and

610 HM-EHEC at Hydrophilic and Hydrophobic Modified Surfaces Monitored by SPR and QCM-
611 D. *Langmuir*, *23*(11), 6148–6155. https://doi.org/10.1021/la063406j
612 Heise, K., Koso, T., Pitkänen, L., Potthast, A., King, A. W. T. T., Kostiainen, M. A., & Kontturi, E.
613 (2019). Knoevenagel Condensation for Modifying the Reducing End Groups of Cellulose
614 Nanocrystals. *ACS Macro Letters*, *8*(12), 1642–1647.
615 https://doi.org/10.1021/acsmacrolett.9b00838
616 Hieta, K., Kuga, S., & Usuda, M. (1984). Electron staining of reducing ends evidences a parallel-
617 chain structure inValonia cellulose. *Biopolymers*, *23*(10), 1807–1810.
618 https://doi.org/10.1002/bip.360231002
619 Howard, S. C., Craig, V. S. J. J., Fitzgerald, P. A., & Wanless, E. J. (2010). Swelling and collapse of
620 an adsorbed pH-responsive film-forming microgel measured by optical reflectometry and
621 QCM. *Langmuir*, *26*(18), 14615–14623. https://doi.org/10.1021/la1023218
622 Kaldéus, T., Nordenström, M., Carlmark, A., Wågberg, L., & Malmström, E. (2018). Insights into
623 the EDC-mediated PEGylation of cellulose nanofibrils and their colloidal stability.
624 *Carbohydrate Polymers*, *181*(September 2017), 871–878.
625 https://doi.org/10.1016/j.carbpol.2017.11.065
626 Karaaslan, M. A., Gao, G., & Kadla, J. F. (2013). Nanocrystalline cellulose/β-casein conjugated
627 nanoparticles prepared by click chemistry. *Cellulose*, *20*(6), 2655–2665.
628 https://doi.org/10.1007/s10570-013-0065-6
629 Koyama, M., Helbert, W., Imai, T., Sugiyama, J., & Henrissat, B. (1997). Parallel-up structure
630 evidences the molecular directionality during biosynthesis of bacterial cellulose.
631 *Proceedings of the National Academy of Sciences*, *94*(17), 9091–9095.

https://doi.org/10.1073/pnas.94.17.9091

Lee, I., Athey, B. D., Wetzel, A. W., Meixner, W., & Baker, J. R. (2002). Structural molecular dynamics studies on polyamidoamine dendrimers for a therapeutic application: Effects of pH and generation. *Macromolecules*, *35*(11), 4510–4520. https://doi.org/10.1021/ma010354q

Lewis, L., Hatzikiriakos, S. G., Hamad, W. Y., & Maclachlan, M. J. (2019). Freeze-Thaw Gelation of Cellulose Nanocrystals. *ACS Macro Letters*, 486–491. https://doi.org/10.1021/acsmacrolett.9b00140

Li, L., Tao, H., Wu, B., Zhu, G., Li, K., & Lin, N. (2018). Triazole End-Grafting on Cellulose Nanocrystals for Water-Redispersion Improvement and Reactive Enhancement to Nanocomposites. *ACS Sustainable Chemistry and Engineering*, *6*(11), 14888–14900. https://doi.org/10.1021/acssuschemeng.8b03407

Lin, F., Cousin, F., Putaux, J., & Jean, B. (2019). Temperature-Controlled Star-Shaped Cellulose Nanocrystal Assemblies Resulting from Asymmetric Polymer Grafting. *ACS Macro Letters*, *8*, 345–351. https://doi.org/10.1021/acsmacrolett.8b01005

Mecke, A., Lee, I., Baker, J. R., Holl, M. M. B., & Orr, B. G. (2004). Deformability of poly(amidoamine) dendrimers. *European Physical Journal E*, *14*, 7–16. https://doi.org/10.1140/epje/i2003-10087-5

Orelma, H., Filpponen, I., Johansson, L., Laine, J., & Rojas, O. J. (2011). Modification of Cellulose Films by Adsorption of CMC and Chitosan for Controlled Attachment of Biomolecules. *Biomacromolecules*, *12*(12), 4311–4318. https://doi.org/10.1021/bm201236a

Potthast, A., Radosta, S., Saake, B., Lebioda, S., Heinze, T., Henniges, U., … Wetzel, H. (2015).

Comparison testing of methods for gel permeation chromatography of cellulose: coming closer to a standard protocol. *Cellulose*, *22*(3), 1591–1613. https://doi.org/10.1007/s10570-015-0586-2

Risteen, B., Delepierre, G., Srinivasarao, M., Weder, C., Russo, P., Reichmanis, E., & Zoppe, J. (2018). Thermally Switchable Liquid Crystals Based on Cellulose Nanocrystals with Patchy Polymer Grafts. *Small*, *14*(1802060), 1–10. https://doi.org/10.1002/smll.201802060

Rodahl, M., Höök, F., Fredriksson, C., Keller, C. A., Krozer, A., Brzezinski, P., … Kasemo, B. (1997). Simultaneous frequency and dissipation factor QCM measurements of biomolecular adsorption and cell adhesion. *Faraday Discussions*, *107*(0), 229–246. https://doi.org/10.1039/a703137h

Sacui, I. A., Nieuwendaal, R. C., Burnett, D. J., Stranick, S. J., Jorfi, M., Weder, C., … Gilman, J. W. (2014). Comparison of the Properties of Cellulose Nanocrystals and Cellulose Nano fi brils Isolated from Bacteria, Tunicate, and Wood Processed Using Acid, Enzymatic, Mechanical, and Oxidative Methods. *ACS Applied Materials and Interfaces*, *6*(9), 6127–6138. https://doi.org/10.1021/am500359f

Sauerbrey, G. (1959). Verwendung von Schwingquarzen zur Wägung dünner Schichten und zur Mikrowägung. *Zeitschrift Für Physik*, *155*(2), 206–222. https://doi.org/10.1007/BF01337937

Schoch, R. L., & Lim, R. Y. H. (2013). Non-interacting molecules as innate structural probes in surface plasmon resonance. *Langmuir*, *29*(12), 4068–4076. https://doi.org/10.1021/la3049289

Shopsowitz, K. E., Qi, H., Hamad, W. Y., & MacLachlan, M. J. (2010). Free-standing mesoporous

silica films with tunable chiral nematic structures. *Nature*, *468*(7322), 422–426. https://doi.org/10.1038/nature09540

Sipahi-Saglam, E., Gelbrich, M., & Gruber, E. (2003). Topochemically modified cellulose. *Cellulose*, *10*, 237–250. https://doi.org/10.1023/A:1025151701985

Sugiyama, J., Persson, J., & Chanzy, H. (1991). Combined Infrared and Electron Diffraction Study of the Polymorphism of Native Celluloses. *Macromolecules*, *24*(9), 2461–2466. https://doi.org/10.1021/ma00009a050

Talantikite, M., Beury, N., Moreau, C., & Cathala, B. (2019). Arabinoxylan/Cellulose Nanocrystal Hydrogels with Tunable Mechanical Properties. *Langmuir*, *35*(41), 13427–13434. https://doi.org/10.1021/acs.langmuir.9b02080

Tao, H., Dufresne, A., & Lin, N. (2019). Double-network formation and mechanical enhancement of reducing end-modified cellulose nanocrystals to the thermoplastic elastomer based on click reaction and bulk cross-linking. *Macromolecules*, *52*(15), 5894–5906. https://doi.org/10.1021/acs.macromol.9b01213

Tao, H., Lavoine, N., Jiang, F., Tang, J., & Lin, N. (2020). Reducing End Modification on Cellulose Nanocrystals: Strategy, Characterization, Applications and Challenges. *Nanoscale Horizons*, *5*, 607–627. https://doi.org/10.1039/d0nh00016g

Tavakolian, M., Lerner, J., Medina, F., Frances, J., Ven, T. G. M. Van De, & Kakkar, A. (2019). Dendrimer directed assembly of dicarboxylated hairy nanocellulose. *Journal of Colloid And Interface Science*, *541*, 444–453. https://doi.org/10.1016/j.jcis.2019.01.100

Tulpar, A., & Ducker, W. A. (2004). Surfactant Adsorption at Solid−Aqueous Interfaces Containing Fixed Charges: Experiments Revealing the Role of Surface Charge Density and

698 Surface Charge Regulation. *The Journal of Physical Chemistry B*, *108*(5), 1667–1676.
699 https://doi.org/10.1021/jp0347668
700 Venditto, V. J., Regino, C. A. S., & Brechbiel, M. W. (2005). PAMAM Dendrimer Based
701 Macromolecules as Improved Contrast Agents. *Molecular Pharmaceutics*, *2*(4), 302–311.
702 https://doi.org/10.1021/mp050019e
703 Villares, A., Moreau, C., & Cathala, B. (2018). Star-like supramolecular complexes of reducing-
704 end functionalized cellulose nanocrystals. *ACS Omega*, *3*(11), 16203–16211.
705 https://doi.org/10.1021/acsomega.8b02559
706 Wang, C., Roman, M., Jiang, F., Heinze, T., Wondraczek, H., Esker, A. R., … Kittle, J. D. (2012).
707 Enhanced Dewatering of Polyelectrolyte Nanocomposites by Hydrophobic Polyelectrolytes.
708 *Langmuir*, *28*(30), 11086–11094. https://doi.org/10.1021/la3016996
709 Wang, X., Ruengruglikit, C., Wang, Y.-W., & Huang, Q. (2007). Interfacial Interactions of Pectin
710 with Bovine Serum Albumin Studied by Quartz Crystal Microbalance with Dissipation
711 Monitoring: Effect of Ionic Strength. *Journal of Agricultural and Food Chemistry*, *55*(25),
712 10425–10431. https://doi.org/10.1021/jf071714x
713 Wintgens, V., & Amiel, C. (2005). Surface plasmon resonance study of the interaction of a β-
714 cyclodextrin polymer and hydrophobically modified poly(N-isopropylacrylamide).
715 *Langmuir*, *21*(24), 11455–11461. https://doi.org/10.1021/la052024v
716 Zhao, Y., Zhang, Y., Lindström, M. E., & Li, J. (2015). Tunicate cellulose nanocrystals:
717 Preparation, neat films and nanocomposite films with glucomannans. *Carbohydrate*
718 *Polymers*, *117*, 286–296. https://doi.org/10.1016/j.carbpol.2014.09.020
719 Zhou, C., Friedt, J., Angelova, A., Choi, K., Laureyn, W., Frederix, F., … Borghs, G. (2004). Human

Immunoglobulin Adsorption Investigated by Means of Quartz Crystal Microbalance Dissipation, Atomic Force Microscopy, Surface Acoustic Wave, and Surface Plasmon Resonance Techniques. *Langmuir*, *20*(14), 5870–5878. https://doi.org/10.1021/la036251d

Zoppe, J. O., Dupire, A. V. M., Lachat, T. G. G., Lemal, P., Rodriguez-lorenzo, L., Petri-fink, A., … Klok, H. A. (2017). Cellulose Nanocrystals with Tethered Polymer Chains: Chemically Patchy versus Uniform Decoration. *ACS Macro Letters*, *6*(9), 892–897. https://doi.org/10.1021/acsmacrolett.7b00383